Journal of Electron Spectroscopy and Related Phenomena 224 (2018) 68–78

Contents lists available at ScienceDirect

Journal of Electron Spectroscopy and Related Phenomena

journal homepage: www.elsevier.com/locate/elspec

Low Dose Photoelectron Spectroscopy at BESSY II: Electronic structure of matter in its native state

Erika Giangrisostomi[a,*], Ruslan Ovsyannikov[a], Florian Sorgenfrei[b], Teng Zhang[c], Andreas Lindblad[c], Yasmine Sassa[c], Ute B. Cappel[c], Torsten Leitner[c], Rolf Mitzner[a], Svante Svensson[c], Nils Mårtensson[c], Alexander Föhlisch[a,b]

[a] Institute Methods and Instrumentation for Synchrotron Radiation Research, Helmholtz-Zentrum Berlin GmbH, Albert-Einstein-Straße 15, 12489 Berlin, Germany
[b] Institute of Physics and Astronomy, University of Potsdam, Karl-Liebknecht-Straße 24/25, 14476 Potsdam, Germany
[c] Department of Physics and Astronomy, University of Uppsala, Box 516, 75120 Uppsala, Sweden

ARTICLE INFO

Article history:
Received 17 December 2016
Received in revised form 27 April 2017
Accepted 26 May 2017
Available online 3 June 2017

ABSTRACT

The implementation of a high-transmission, angular-resolved time-of-flight electron spectrometer with a 1.25 MHz pulse selector at the PM4 soft X-ray dipole beamline of the synchrotron BESSY II creates unique capabilities to inquire electronic structure via photoelectron spectroscopy with a minimum of radiation dose. Solid-state samples can be prepared and characterized with standard UHV techniques and rapidly transferred from various preparation chambers to a 4-axis temperature-controlled measurement stage. A synchronized MHz laser system enables excited-state characterization and dynamical studies starting from the picosecond timescale. This article introduces the principal characteristics of the PM4 beamline and LowDosePES end-station. Recent results from graphene, an organic hole transport material for solar cells and the transition metal dichalcogenide MoS_2 are presented to demonstrate the instrument performances.

1. Introduction

Photoelectron spectroscopy (PES) is one of the main tools for the study of the electronic properties of free molecules, liquids and solid samples [1]. The method originated from the pioneering work of Prof. Kai Siegbahn (Nobel Prize for Physics in 1981) and his co-workers [2–4] and – since then – the field has developed rapidly. One fundamental milestone was the discovery in 1963 of the core electron binding energy chemical shift [5], that motivated the acronym Electron Spectroscopy for Chemical Analysis (ESCA). A recent review of this early period can be found in Ref. [6]. The first detectors made it possible only to analyze high kinetic energy electrons excited by hard X-ray sources. At the beginning of the 1960's, detectors for low energy electrons became available and it was found that resonant emission from ultra-violet lamps could be used to study high-resolution valence electron spectra [7]. From then on, the field of photoelectron spectroscopy was divided in the two branches of Ultraviolet Photoelectron Spectroscopy (UPS) and X-ray Photoelectron Spectroscopy (XPS) based on the employed excitation source. XPS was mainly focusing on core levels, whereas UPS was addressing valence states and it triggered the development of instrumentation to study the energy- and momentum-resolved band structure of solids, *i.e.* Angle-Resolve Photoelectron Spectroscopy (ARPES).

The introduction of synchrotron radiation as a photon source – with its properties of high brilliance, strong collimation, pulsed time structure, tunable energy, and defined polarization state – has boosted the field enormously. The dramatic increase in brilliance of synchrotron radiation over the years has in general enabled more and more sophisticated high resolution studies [8]. However, there are certain classes of materials where the higher brilliance, rather than being an advantage, turns into a drawback due to radiation-induced sample damage [9]. A lower photon flux is beneficial for probing these materials, but also non-conductive samples inasmuch as it reduces the problem of sample charging. In such cases, one has to resort to other means of improving the efficiency of the measurements.

An obvious route is to improve the detection efficiency of the electron spectrometer. An improved detection efficiency by a factor of roughly two to three orders of magnitude with respect to more conventional hemispherical analyzers without loss of

* Corresponding author.

https://doi.org/10.1016/j.elspec.2017.05.011

resolution is the key feature of the novel Angular Resolved Time-of-Flight (ArTOF) electron analyzer [10]. The very high transmission (about 13%) and the collection of electrons over a broad solid angle (up to ±30°) allow to compensate for the increase in collection times that results from a decrease in the X-ray flux. Moreover, if sample degradation occurs over time, it can be easily tracked and sorted out also after the measurements since the collected kinetic energies and emission angles for each individual event are stored in a time-tagged manner.

Time-of-flight techniques call for a pulsed excitation source. Specifically, pulse repetition rates not faster than a few MHz are demanded in order for electrons from different photoemission events to be unambiguously interpreted and pulse durations not longer than approximately tens of ps are required for optimum resolution (below 1 meV at few eV kinetic energies). In this respect, the third-generation synchrotron BESSY II in Berlin, Germany and the PM4 beamline therein represent an ideal facility. In fact, BESSY II normally operates in the so-called hybrid mode, where a camshaft bunch of 4 mA[1] at the center of a 200 ns wide gap in the multi-bunch pattern is filled and topped up. Furthermore, the optical layout of the PM4 beamline is such that a fast mechanical chopper can isolate – out of the multi-bunch train – the camshaft pulse, conveniently featuring a duration of about 70 ps FWHM and a repetition rate of 1.25 MHz.

In the present paper, we describe the LowDosePES end-station permanently installed and operative at the BESSY II PM4 beamline and propose a selection of exemplary experiments.

2. Description of the beamline

PM4 is a dipole beamline located at section 10.1 of BESSY II. Its optical layout is sketched in Fig. 1.

Monochromatization is performed by a plane grating monochromator (*M2* and *G* in the figure) operated with a collimated beam [11]. Three plane gratings with 150, 360 and 1228 l/mm can be interchanged covering the photon energy ranges 7–1000, 18–2000 and 75–2000 eV respectively at a constant focal distance $c_{ff} = cos\beta/cos\alpha$ of 2, where α is the incident angle and β is the diffraction angle. Slightly changed photon energy ranges will result from a different choice of the c_{ff} value, that may be dictated by the need for higher resolution (higher c_{ff}) or higher spectral purity, i.e. better suppression of higher order light (lower c_{ff}). Selected plots illustrative of the interconnection between these parameters can be found in the beamline documentation page at the Helmholtz Zentrum Berlin (HZB) website [12].

The toroidal mirror *M1* focusses the X-ray beam horizontally about 90 cm beyond the intermediate vertical focus created by the cylindrical mirror *M3* at the position of the exit slit, a position about 287 cm ahead of the focal spot produced by the toroidal mirror *M4* at the center of the main experimental chamber. We estimated the final focus to be 95 μm-wide × 65 μm-high in the presence of a 100 μm-wide slit at the intermediate focus and 170 μm-wide × 75 μm-high in the absence of it.

Originally the beamline was indeed designed to host two types of experiments. A reflectometer [13] used by the Institute for Nanometre Optics and Technology of HZB for characterization of optical surfaces was placed at the intermediate focus, while – at the final focus – the SURICAT end-station [14] dedicated to SURface Investigation and CATalysis was installed. With the introduction of an ArTOF, the SURICAT end-station has undergone a substantial upgrade into what is now the LowDosePES end-station. At the same time, the reflectometer has moved to another beamline and the aforementioned chopper has taken its place.

As described in detail in Ref. [15], the chopper consists of a wheel made of a high-strength aluminum alloy having at its outer rim 1252 high-precision slits of 70 μm width. It is kept under vacuum, levitated by magnetic bearings, and rotates frictionless at a peripheral velocity of 1063 m/s. The motion is synchronized to the master clock of the storage ring in such a way that all photon bunches except the camshaft ones are cut by the convolution of the rotating chopper slits with a fixed slit positioned just downstream.

The fast mechanical chopper represents only one way of achieving single pulse picking at MHz frequencies. Necessary requirements for its use are a small enough horizontal intermediate focus in the beamline and a wide enough gap around the camshaft pulse in the synchrotron filling pattern. Aside from the single-bunch operation mode of the ring – which would hamper the majority of synchrotron users, more interested in the high current than in the pulsed structure – alternative methods to operate the ArTOF at the required lowered frequency have been demonstrated. One method is pulse picking by resonant excitation (PPRE) [16]. This is also being exploited at BESSY II and is the reason for the additional high current bunch visible in Fig. 2 close to the right end of the filling gap, but it can only be implemented at an undulator beamline. Another method is based on gating of the detector [17]. In this case, however, the sample is experiencing the X-ray dose from the full multi-bunch pattern.

Fig. 2 shows a drawing of the chopper together with an illustration of its effect on the time structure of the X-ray beam. The latter information is readily available by letting photons scatter by whatever surface on the experimental chamber manipulator towards the ArTOF, that will only detect photons if high negative voltages are applied to its lenses and detector. A fixed chopper slit of 100 μm width results in an usually satisfactory compromise between purity in the time structure and intensity of the beam, characteristics that can be appreciated from the plots in Figs. 2 and 3 respectively.

The graph on the upper panel of Fig. 3 shows the photon flux as a function of photon energy for the three gratings (red, green and blue colors) at two commonly used c_{ff} values (solid and dotted lines). The corresponding calculated photon energy bandwidth is shown on the lower panel of the same figure. Flux measurements are provided by a calibrated GaAsP photodiode placed right after the last optical element of the beamline. The reported curves refer to the usual situation where the single bunch current is about 4 mA, the exit slit is open to 100 μm and the chopper is running at full operational speed with a 100 μm wide slit inserted behind. Under the same ring current and exit slit settings but with the chopper at rest and its outer slit removed, the photon flux has been measured to be roughly 100 times higher.

3. Description of the end-station

The end-station is conceived as a modular system consisting of the interconnected preparation and measurement ultra high vacuum chambers shown in Fig. 4.

3.1. Main chamber

The main measurement chamber (A) is equipped with a Scienta ARTOF-2 electron analyzer and also with the Scienta SES100 inherited from SURICAT.

The SES100 is a hemispherical electron analyzer with a 2D detector consisting of two micro-channel plates (MCP) in Chevron configuration, a phosphor screen and a CCD camera. It can be operated in three angle-resolved modes or in the transmission-optimized mode with no particular demand on the time structure

[1] To avoid confusion: at most storage rings it is of use to express the bunch current in mA; for FELs the bunch charge in nC is normally given. For a comparison it is necessary to divide the former number by the ring frequency.

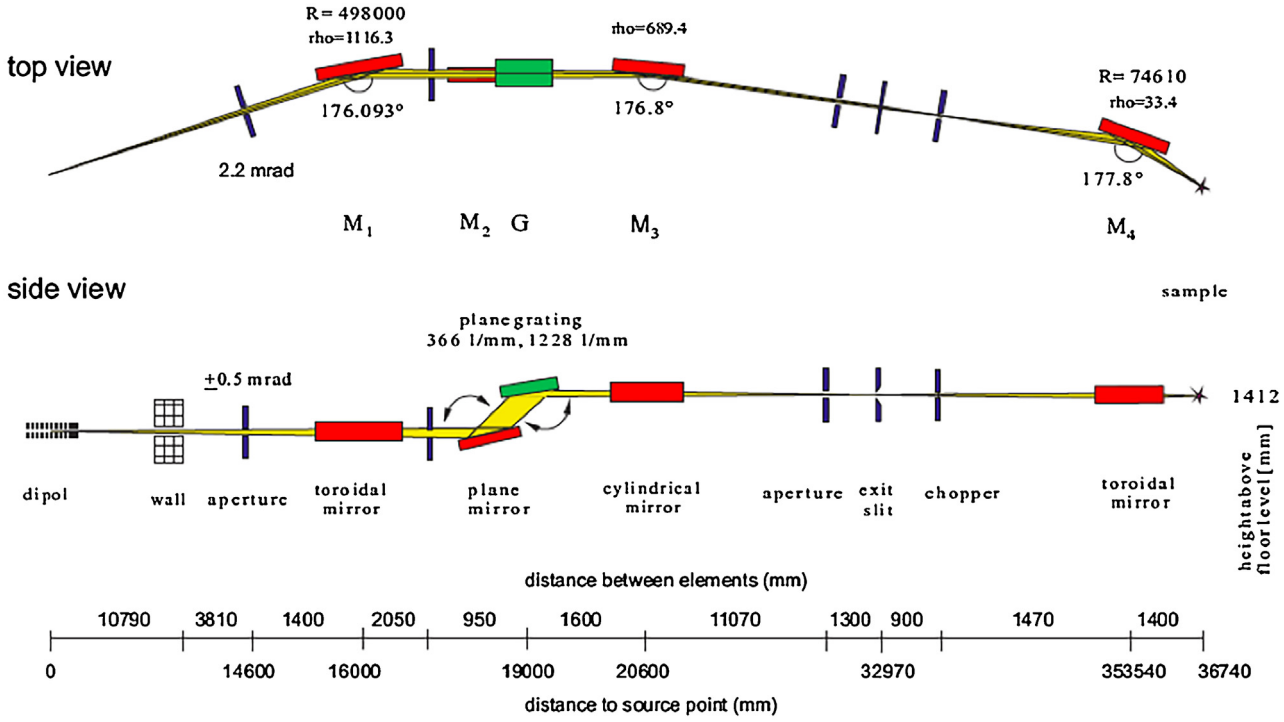

Fig. 1. Optical layout of the plane grating monochromator beamline PM4 at BESSY II [9]. Note the sagittal and meridional intermediate foci, the former at the position of the exit slit for monochromatization and the latter at the position of the chopper for 1.25 MHz pulse extraction.

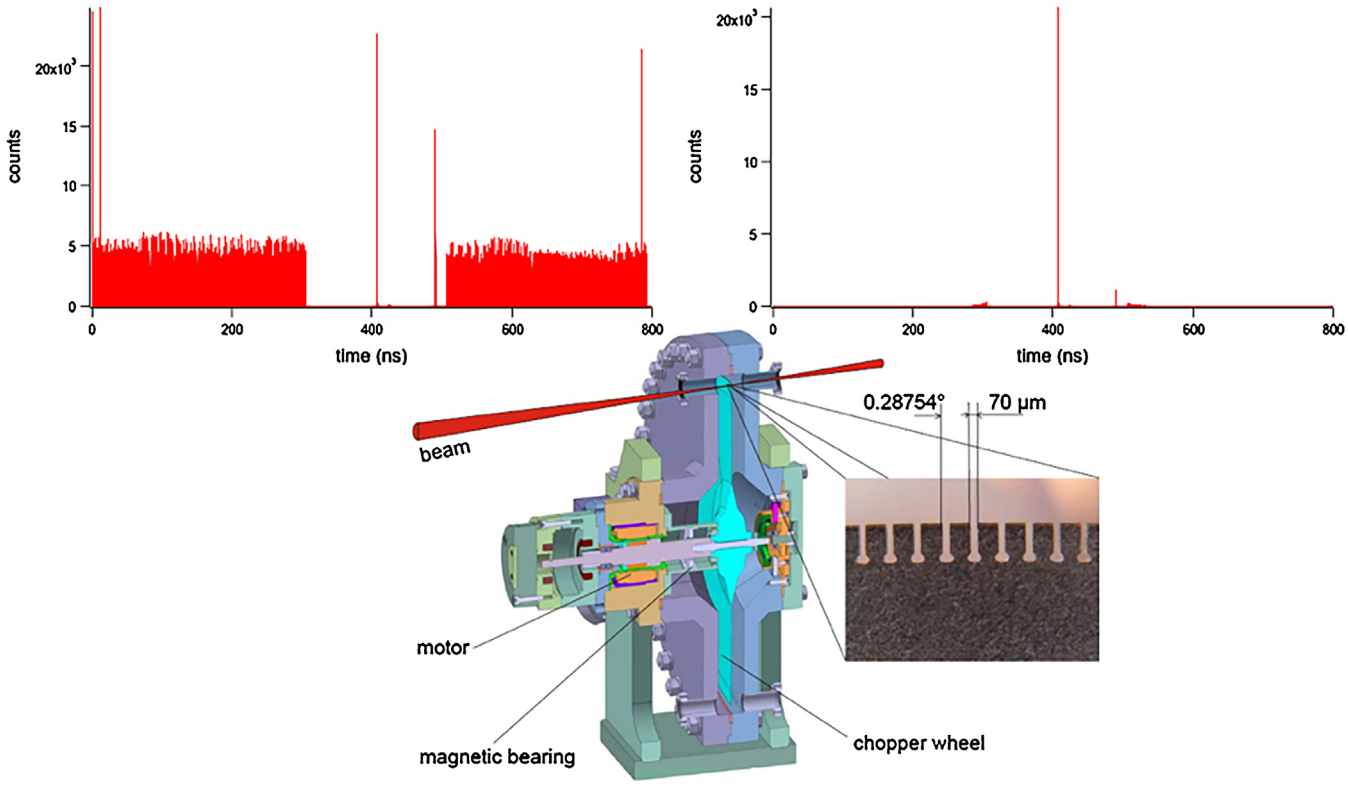

Fig. 2. 3D drawing of the chopper (bottom) [12] and time structure of the synchrotron light before (top left) and after (top right) it as measured by the ArTOF. The chopper is synchronized with the hybrid bunch in the middle of the gap characteristic of the multi-bunch filling pattern of BESSY II.

of the light source (*i.e.* it can be used in multi-bunch mode without the chopper running).

When low irradiation conditions are not required and the angular information is not of interest, the latter mode of the SES100 offers the greatest efficiency, especially at higher kinetic energies. In the other cases, the SES100 is less competitive with respect to the ArTOF-2. In fact, only one direction of the detector corresponds to the angularly dispersed signal in a hemispherical analyzer, the

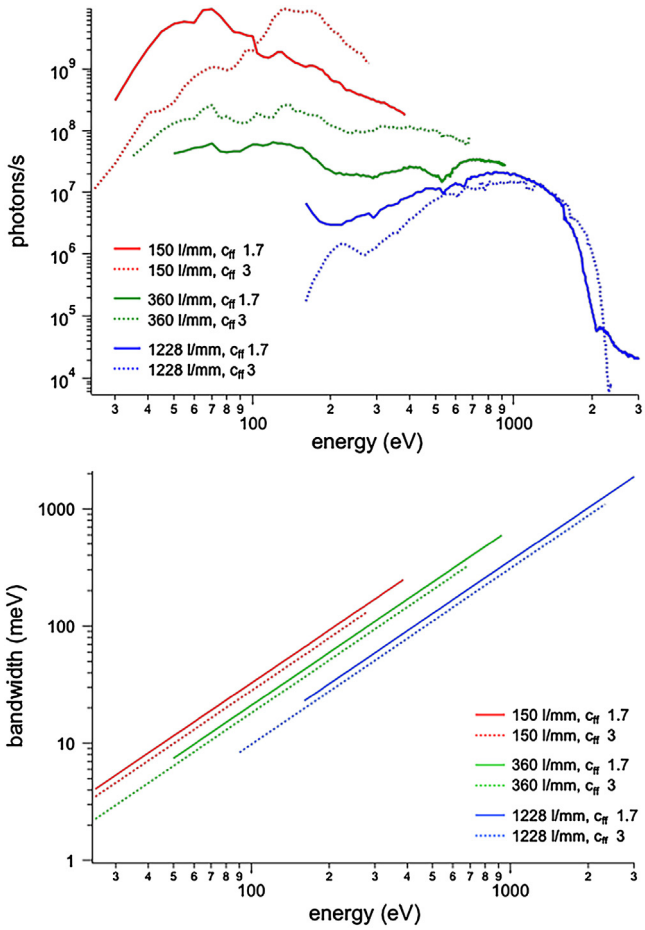

Fig. 3. Measured photon flux (top) and calculated energy resolution (bottom) for the PM4 beamline as a function of photon energy.

other direction being the one of energy dispersion. In an ArTOF, on the other hand, the kinetic energy is determined from the time-of-flight, therefore both directions of the detector can be exploited to provide angular information. In our instrument, the 2D time-resolved detector is a delay line from Roentdeck made of two Chevron stacked MCPs and two grids of wires: the MCP provides the arrival times of the electrons, whereas measurement of the arrival times of the electron pulses at the two ends of the wires yields the electron angular coordinates. Moreover, in an ArTOF there is no need for the entrance slit which is instead mandatory in a hemispherical electron analyzer to achieve high resolution. As a consequence, all electrons within the whole acceptance cone of, in our case,[2] ±15° are collected, which explains the high transmission and leads to the possibility of recording full band maps (linear momentum in two directions and binding energy) over extended regions of the Brillouin zone without having to rotate the sample. A previous publication [10] offers to the interested reader a detailed comparison between the information rates of the ArTOF 10k and the Hemispherical R4000 WAL for selected kinetic energies and energy resolutions.

The main chamber is built of μ-metal in order to guarantee optimal shielding from magnetic stray fields, and is kept at a base pressure lower than $5 \cdot 10^{-10}$ mbar. It is provided with a 4-axis (X, Y, Z and azimuthal angle ϕ) manipulator (Omniax from Vacgen) ending with a cryostat (ST-400 from Janis Research Company) that allows measurements to be performed at a sample temperature ranging from 500 K to 10 K. The sample is mounted at the end of the cryostat cold finger on a home-made Cu holder compatible with standard Omicron sample plates. The holder is connected to ground potential so that collection of the drain current upon X-ray irradiation provides a measure of the X-ray absorption near edge structure (XANES) spectrum in total electron yield.

Anchored at the bottom of the sample holder are a polycrystalline Au foil and an unpolished Yttrium Aluminum Garnet (YAG) crystal for fast check of the X-ray energy calibration and focal spot (looking at the visible emission with a telemicroscope camera), respectively. A couple of cameras with different fields of view, resolutions and sensitivities are available at the main chamber to visually assist sample transfer and for identification of suitable measurement positions on the sample.

3.2. Auxiliary chambers

Additional tools for sample preparation and characterization are hosted in auxiliary chambers.

The top chamber (B) is endowed with an MCP LEED (BDL800IR from OCI Vacuum Microenigineering) for characterization of surface quality and a mass spectrometer (Microvision 2 from MKS Instruments) for analysis of the residual gases. Evaporation of non-contaminating molecules can be made here in the course of a measurement or otherwise at a second side chamber (C), reaching a vacuum level better than $5 \cdot 10^{-10}$ mbar. In the latter, the manipulator has six sample storage places, two of which can be heated resistively up to about 900 K. Electron bombardment heating will

[2] An acceptance cone of ±30° is featured by a more recent version of the instrument to which one can upgrade.

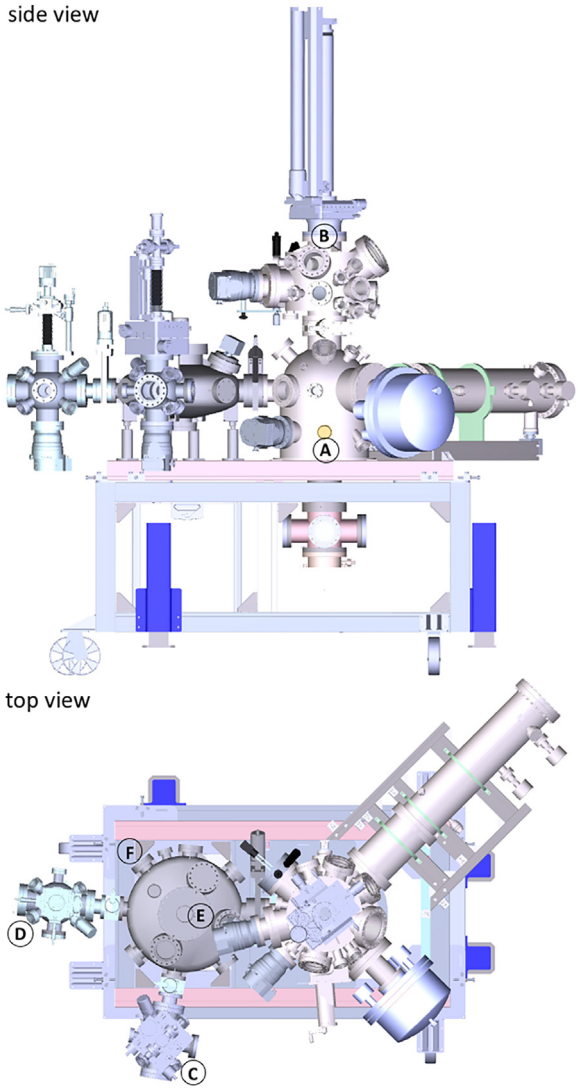

Fig. 4. Sketch of the LowDosePES end-station: (A) Main experimental chamber equipped with ArTOF and hemispherical electron analyzers; (B, C) clean sample preparation chambers; (D) organic sample preparation chamber and load lock; (E) transfer chamber with free ports for additional preparation chambers (F).

soon also be available at one of these locations in order to allow flashing at higher temperatures. A sputter gun (IQE 11/35 from Specs) is installed for crystal cleaning, together with a couple of leak valves (one used for Ar ion sputtering, one used for dosing of other gases) and a quartz microbalance to monitor thickness growth during evaporation. A wobble stick for sample cleaving is also available.

A third side chamber (D), easily reaching pressures lower than $5{\cdot}10^{-8}$ mbar without bake-out, serves the dual purpose of a load lock chamber for introducing samples and of a preparation chamber for evaporation of organics or other similarly contaminating materials. It has storage place for six samples and several free ports for mounting replaceable equipment from the users.

Samples can be readily transferred from the load lock chamber to the other preparation chambers and to the main chamber via a radial distribution system (E, UFO from Prevac). The latter also offers the opportunity to install further preparation chambers possibly brought by the users.

3.3. Software

Most of the beamline hardware is handled by the distributed control system EPICS, which also monitors and archives relevant parameters of the synchrotron radiation beam. Exceptions are the electron analyzers, operated with the acquisition software provided by the manufacturing companies. In addition, an Igor-based package of programs for real-time analysis of ArTOF data is at the disposal of all users.

The ArTOF Studio Console (ASC) from Scienta stores as binary files the set of (t_0, t, X, Y) data – where t_0 and t are the arrival times of the excitation pulse at the sample and of the photoelectron at the detector respectively, and X and Y are the spatial coordinates of the photoelectron on the detector. A graphical interface allows loading either these raw data or the converted datasets (E_{kin}, ϕ, θ) or (E_{kin}, k_X, k_Y) for a straightforward visualization of the measured signal in terms of electron kinetic energies E_{kin} and emission angles ϕ and θ or K-space coordinates k_X and k_Y.

As visible by the snapshot in Fig. 5, a 3D browser displays the three two-dimensional plots E_{kin} vs $\phi(/k_X)$, E_{kin} vs $\theta(/k_Y)$ and $\phi(/k_X)$ vs $\theta(/k_Y)$ at given values of the third dimension $\theta(/k_Y)$, $\phi(/k_X)$ and E_{kin} respectively. A cursor can be slided across the latter coordinate and one can observe how the 2D plots change right away. Integration of the 2D plots over the third coordinate is also implemented. Additionally, it is possible to select an arbitrary direction in a 2D plot and display the counts as a function of this axis and the third dimension. The range and binning size for each coordinate can be chosen at will upon loading. *A posteriori*, the coordinate system can be translated and rotated for finer alignment with respect to the measured symmetry features. Various normalization procedures are available, among which one that allows to correct possible spatial inhomogeneities of the detector.

4. Selected results

4.1. Angle-resolved photoelectron spectroscopy on graphene

Owing to its out standing properties which hold exciting promises for novel electronics and spintronics applications, graphene is receiving enormous attention in the scientific community. It is therefore no surprise that its peculiar electronic structure has been extensively studied by ARPES. This reason and the fact that its surface is relatively inert made graphene eligible as a test sample for ArTOF performance checks at our end-station.

Fig. 5 and Fig. 6 represent an example of ARPES measurement realized at the LowDosePES end-station with the ArTOF spectrometer on a commercial sample (from GrapheneSiC AB) of graphene epitaxially-grown on the Si-terminated surface of a 4H-SiC(0001) substrate. The sample was held at a temperature of about 70 K and irradiated with a beam of $\approx 7{\times}10^7$ 80 eV photons/s. Data for 20° off-normal emission were acquired for 12 h at a rate of ≈31,200 counts/s.

Fig. 5 shows the Fermi surface (left panel) and the dispersion of the bands along the k_X *[K-Γ-M]* and k_Y *[K-M]* directions (middle and right panels, respectively). Results are in agreement with the literature [18,19], including the shift of the Dirac point relative to the Fermi energy caused by electron doping from the substrate [20]. The main advantage in our case is that no rotation of the sample was needed to measure all over the Brillouin zone, which allows for a straightforward representation of the data.

For example, the same dataset is shown in Fig. 6 rendered in a 3D plot using Matlab. Here the distribution of electrons in the $[E_{kin}, k_X, k_Y]$ space is given as a logarithmic colormap, with higher densities encoded by warmer colors. Momentum distribution maps (MDM) are displayed at kinetic energies 72, 73, 74 and 74.9 eV, whereas the

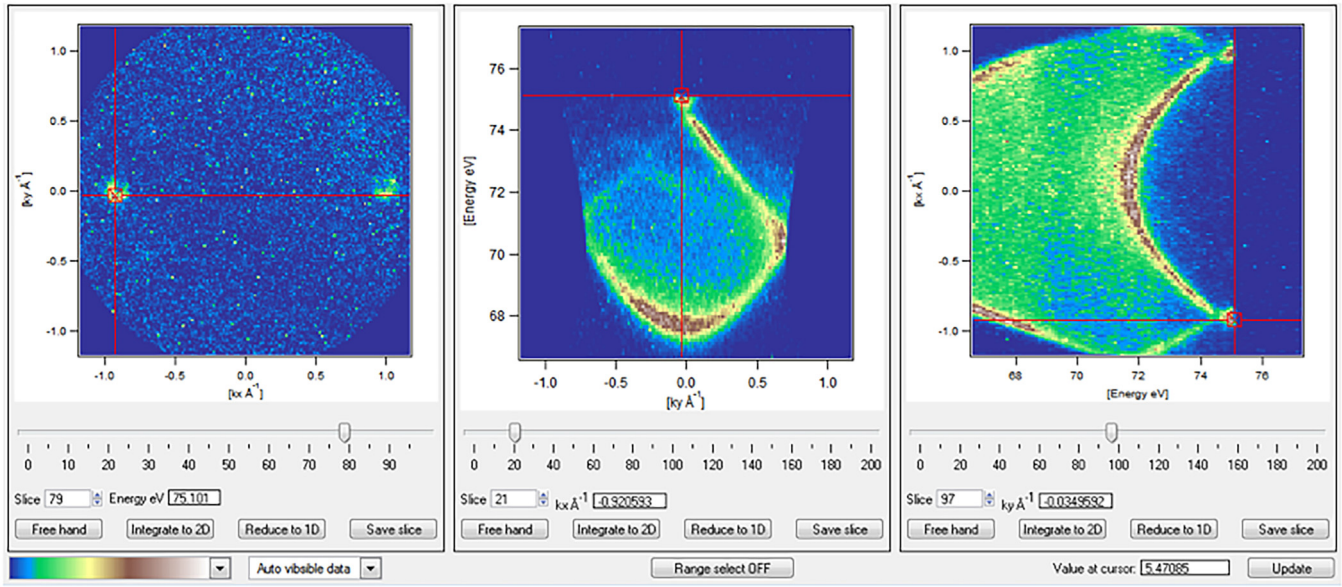

Fig. 5. Screenshot from the IGOR program allowing for real time visualization of processed ARPES data. The left panel represents the Fermi surface of graphene with visible shadow cones. The middle and right panels show a cut along the k_Y (vertical red line in the left panel) and k_X (horizontal red line in the left panel) directions, respectively. (For interpretation of the references to colour in this figure legend, the reader is referred to the web version of this article.)

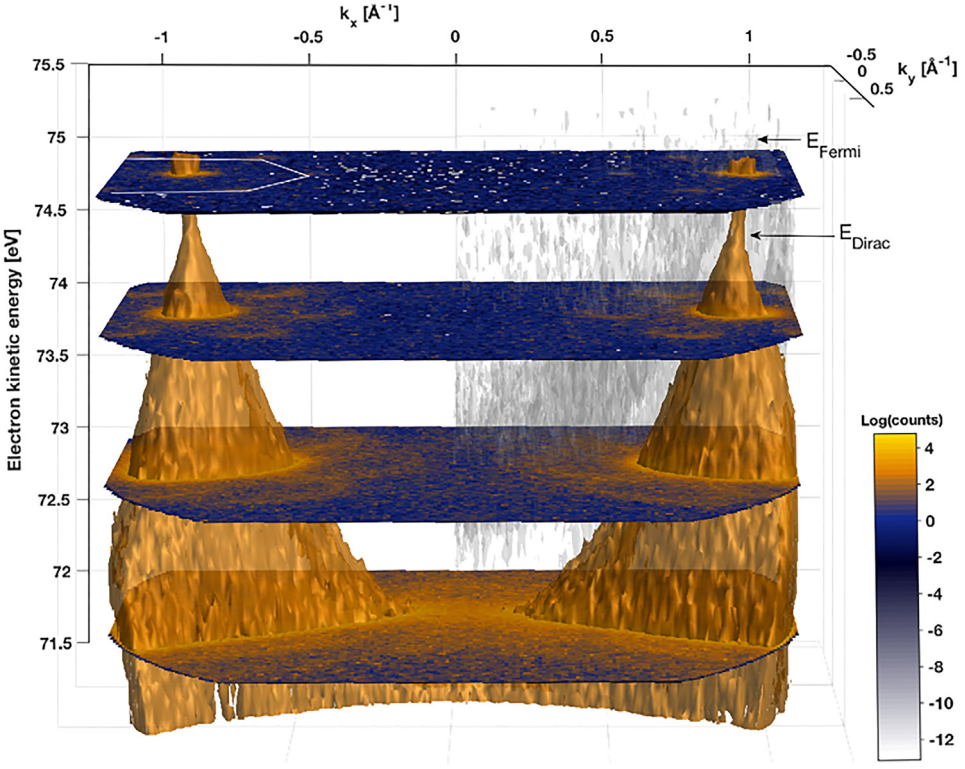

Fig. 6. 3D representation of the valence band of graphene. Black arrows indicate the positions of the Fermi and Dirac energies; white lines highlight the shadow cones. The color scale is logarithmic. Keep in mind that electron kinetic energies and perpendicular and parallel momenta are recorded simultaneously without moving the sample or the detector.

rest of the volume only encompasses the highest intensity points (in the right part of the figure an isosurface at 4 orders of magnitude lower intensity than the maximum is included, which is instead filtered out in the left part of the figure).

This way of handling the data can aid in highlighting specific faint features of the band structure. One such feature is the anisotropy of the energy dispersion around the Dirac points at *K* and *K'*, which is known as trigonal warping and derives from second order corrections to the tight-binding expansion [21]. Another feature which can be nicely observed are the shadow cones that have an origin at about 0.45 $Å^{-1}$ away from the Dirac points, compatibly with the 6×6 corrugation of the C-rich buffer layer at the interface between the graphene and the silicon carbide surfaces [22].

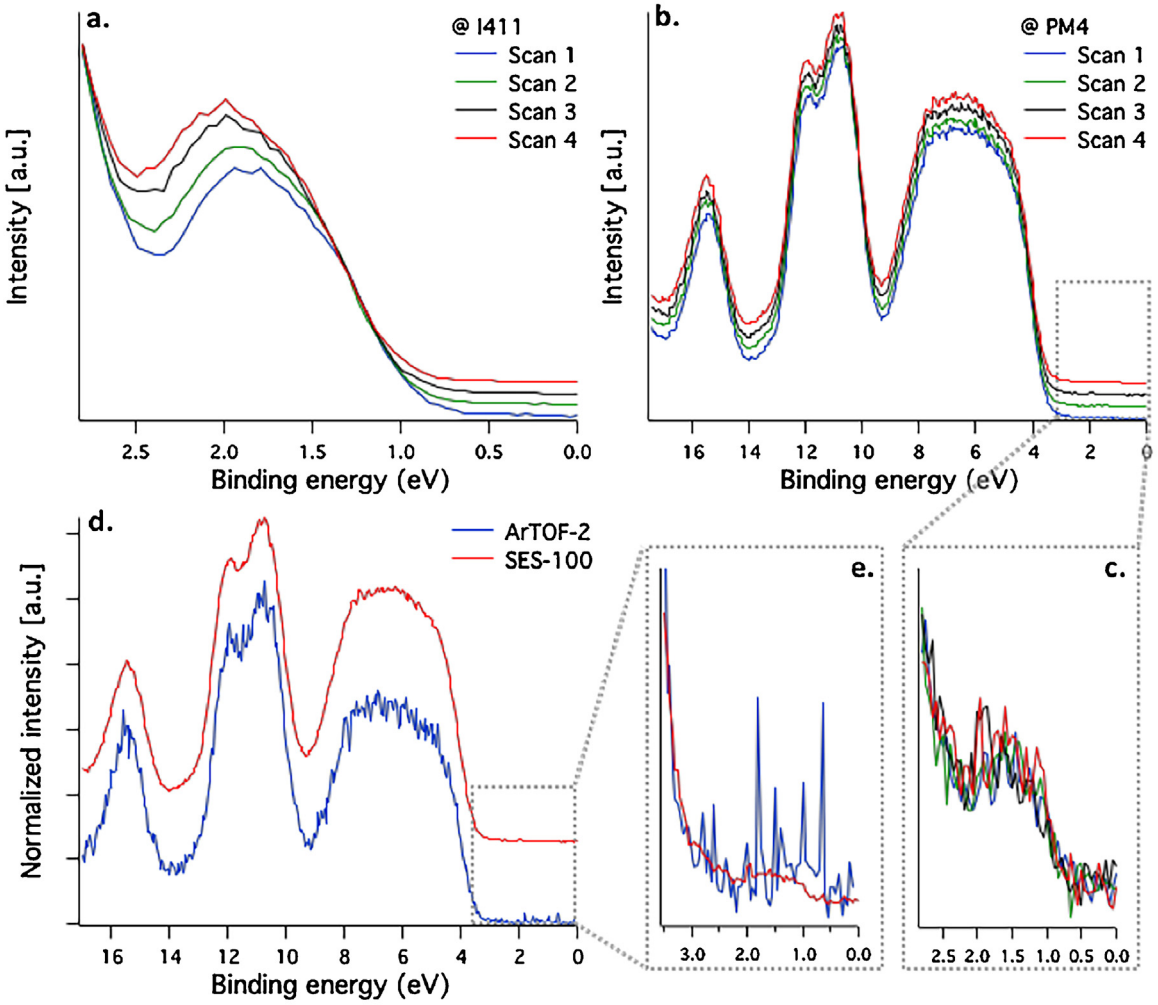

Fig. 7. Valence spectra of LiTFSI-doped spiro-MeOTAD as measured by different instruments: a.) 4 consecutive 1 min scans collected at the I411 beamline with a SES4000 analyzer, showing signatures of radiation damage; b.) 4 consecutive 10 min scans collected at the PM4 beamline with an ArTOF-2 analyzer (zoom in the HOMO region shown in c.), showing no signature of radiation damage; d.) comparison of 10 min spectra acquired at the PM4 beamline with ArTOF-2 and SES100 analyzers (zoom in the HOMO region shown in e.), highlighting the high transmission capabilities of the former over the latter under equal measurement conditions. The example illustrates the importance of minimizing X-ray dose and maximizing detection efficiency in order to determine the native state of radiation-sensitive samples.

4.2. Low-dose photoelectron spectroscopy on LiTFSI-doped spiro-MeOTAD

In Fig. 7 a second example is reported to illustrate the strength of the ArTOF spectrometer when it comes to experiments that demand a low irradiation dose. The sample is a thin film of 2,2′,7,7′-tetrakis(N,N-di-p methoxyphenylamine)-9,9′-spirobifluorene (spiro-MeOTAD) doped with Li-bis(trifluoromethanesulfonyl)-imide (LiTFSI) deposited on a mesoporous TiO_2 substrate, an organic material of interest as hole conductor in dye-sensitized and perovskite-based solar cells [23,24].

Even a short exposure to the brilliant X-rays of the I411 beamline at the MAX II storage ring in Lund, Sweden [25] caused the highest occupied molecular orbital (HOMO) peak to irreversibly shift over time towards lower binding energies as an effect of the degradation of the TFSI ion (panel *a.*). The same sample remained instead unaltered under much more prolonged exposure to the X-ray beam (at least 5 h) at the PM4 beamline (panels *b.* and *c.*). Also the fact that the feature between 10 and 13 eV binding energy – which we assign to F 2p – does not decrease in intensity demonstrates the stability of TFSI in the latter case. Furthermore, while the spectra measured at PM4 are energy-calibrated to the Fermi edge of a gold reference, such a calibration is prevented by sample charging for the spectra measured at I411, which were therefore calibrated to the Ti 3p peak of the substrate.

In such low flux conditions (about 6.5×10^6 photons/s), the high throughput of the ArTOF (resulting here in about 7000 counts/s in the binding energy region 0–17 eV) as compared to more standard hemispherical analyzers is a remarkable figure of merit, as demonstrated by panels *d.* and *e.* of Fig. 7 that compare valence band spectra collected with the two spectrometers at equal beamline settings and exposure times. While the main features of the valence region are visible with both spectrometers, the photoemission peak of the spiro-MeOTAD HOMO level at about 1.5 eV binding energy can only be detected clearly with the ArTOF.

5. Integrated laser facility

The high count rate and high time resolution featured by its delay line detector naturally make the ArTOF electron spectrometer appealing for time-resolved photoemission studies.

In principle, any process developing on a timescale longer than the BESSY II single pulse frequency of 1.25 MHz (*i.e.* 800 ns) could be monitored with suitable time resolution. In practice, the collection time for getting a reasonable statistic will be the defining factor for the temporal resolution with which the process can be monitored.

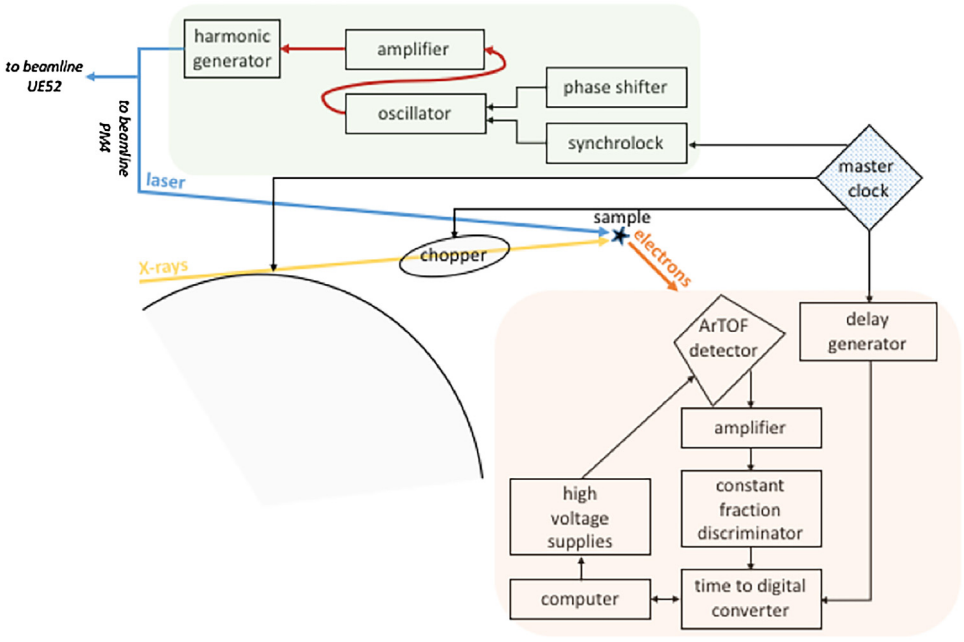

Fig. 8. Timing scheme for the instruments demanding synchronization to the synchrotron radiation emission: chopper, ArTOF (orange area) and laser (green area) systems. (For interpretation of the references to colour in this figure legend, the reader is referred to the web version of this article.)

Thus here is another area where the high detector efficiency plays an important role. Simple applications of this concept could be spectroscopic investigations of adsorption and desorption during the course of molecular exposure and substrate heating respectively, or tracing of sample degradation as an effect of exposure to the X-ray beam or to residual gases in the chamber. In relatively slow processes like the latter, it is not the short acquisition time and fast readout that matter, but rather the possibility to verify a posteriori when the sample started to alter unacceptably, and sort the measurements accordingly.

Another type of time-resolved spectroscopy – applicable to different classes of phenomena – is based on the pump-probe approach, wherein the X-ray beam is preceded by a stimulus occurring at a specific and tunable distance in time, and so repetitively for each X-ray pulse reaching the sample. In order to allow this type of studies, a new laser facility has recently been set up, which is serving the PM4 beamline in alternation with the nearby beamline UE52.

The laser in question is a customized version of the Tangerine model from the company Amplitude Systemes. The attractive feature of this ytterbium-doped fiber laser is that the short pulse duration and high energy per pulse normally sought in pump-probe experiments come combined with high repetition rates. More precisely, the laser specifications are as follows: a fundamental wavelength of 1030 nm, a pulse length tunable from 330 fs to 10 ps, an average power of 30 W and a repetition rate tunable – at a pre-amplification stage – from 200 kHz to 2 MHz, with resulting pulse energies spanning from 150 μJ at 200 kHz to 15 μJ at 2 MHz. A second acousto-optic modulator after the amplication stage can further reduce the repetition rate down to a single pulse at unaltered pulse energy and correspondingly reduced average power. The customization resides in integrated modules for synchronization and phase shifting with respect to an external source (the storage ring of BESSY II in this case).

Fig. 8 graphically summarizes the signals flow that ensures proper timing between the emission of the X-rays, the single bunch chopping of the X-rays, the laser emission and the collection of electrons from the X-ray induced photoemission of the laser-excited sample.

The laser is located inside a dedicated hutch where appropriate beta barium borate (BBO) crystals can be used to generate second, third or fourth harmonics of the fundamental wavelength, if wished. The beam is then directed to either one or the other beamline traveling inside vacuum tubes deflected by a series of multilayer mirrors having a high-reflection coating specific for the four harmonics. At PM4 the laser beam ends up on a curtain-shielded optical breadboard where lenses bring it to have a focus on the sample at the same position of the X-rays focus and where more beam conditioning can be done, like tuning of the spot size or modification of the polarization. The laser and the X-rays reach the sample at about the same angle, the latter going through and the former being reflected by a piezo-actuated mirror with a hole in the middle, which is hosted in a small vacuum chamber placed between the chamber of the last refocusing X-ray mirror and the main experimental chamber, as sketched in Fig. 9.

5.1. Time-resolved photoelectron spectroscopy on MoS_2

Integration of the pulsed laser to the beamline is a recent upgrade. Below we present a preliminary result from the commissioning where we have explored the dynamical response of a multilayer molybdenum disulphide sample to laser pumping. On panel *a.* of Fig. 10, the S $2p_{1/2}$ and S $2p_{3/2}$ core level spectra are shown as a function of pump-probe delay for the case of a pump beam of 515 nm wavelength, 60 mW power and 1.25 MHz repetition rate focused to a spot of 220 μm diameter (corresponding to an energy per pulse of ≈ 48 nJ, energy density of ≈ 126 $\mu J/cm^2$ and power density of ≈ 158 W/cm^2). Each curve was measured for 2 min at a flux of about 2×10^7 X-ray photons/s, yielding about 800 counts/s in the spectral region of interest, so that the whole scan from −600 ps to +1000 ps at a step of 50 ps took slightly more than one hour.

Around zero pump-probe delay, both peaks undergo a pronounced shift to higher kinetic energies accompanied by an increase in the width. As clear from the Gaussian fit results reported in panel *c.* of Fig. 10, the peak widths recover very quickly whereas the recovery of the peak shifts take considerably longer and is not complete within the 800 ns available before the next couple of

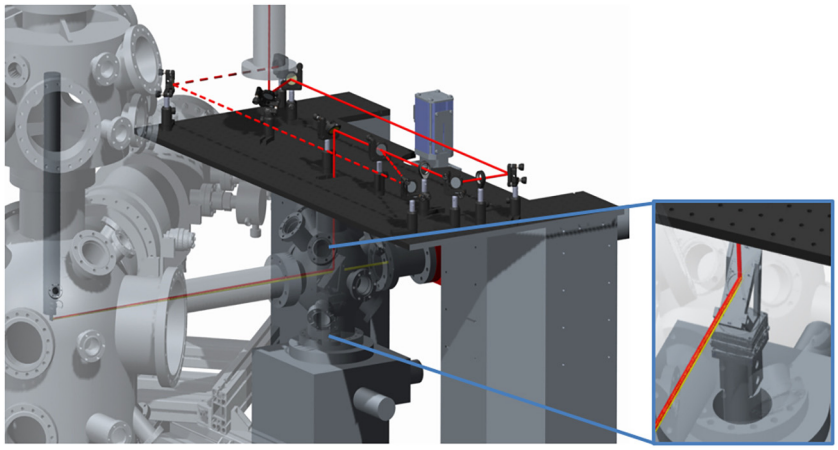

Fig. 9. Setup for coupling the laser to the end-station. On the right, a zoom of the last laser steering mirror. The X-ray beam from BESSY II is depicted in yellow, the laser beam in red. The solid and dashed lines departing from a beamsplitter on the optical breadboard represent respectively the main portion of the laser beam which is reaching the sample position and a small fraction of it that, after a path of equal length, reaches a beam profiler camera for spot size determination. (For interpretation of the references to colour in this figure legend, the reader is referred to the web version of this article.)

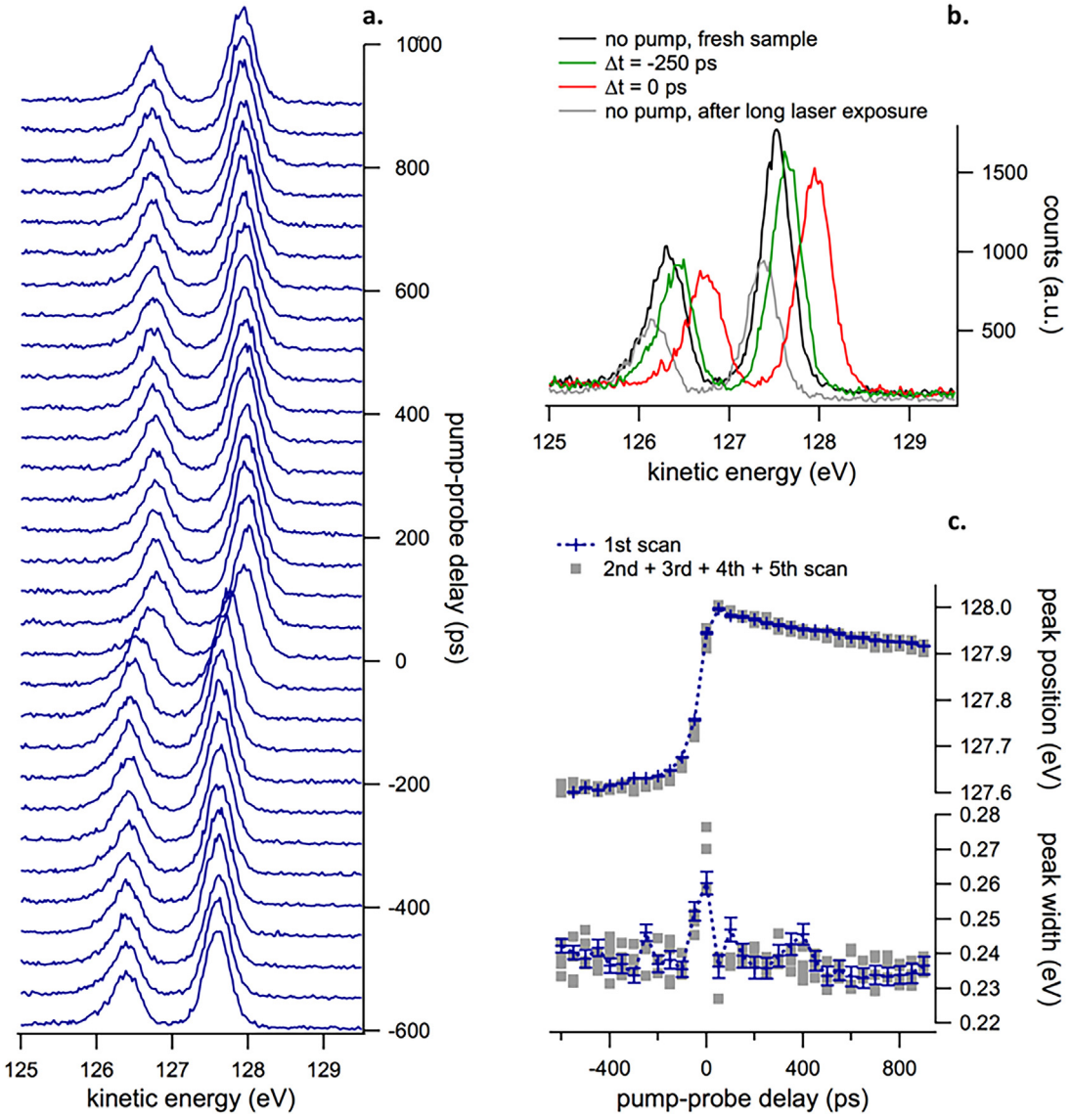

Fig. 10. Photo-induced dynamics in crystalline MoS_2 probed by time-resolved photoelectron spectroscopy on a picosecond to nanosecond timescale.

pump and probe pulses at the chosen repetition rate of 1.25 MHz. This is the reason why the spectra at negative pump-probe delays are also slightly shifted to higher kinetic energies with respect to the spectrum of the un-pumped sample (green vs black curves in panel *b.*). When comparing the un-pumped spectra of the fresh sample and of the laser-exposed sample (black vs grey curves in the same panel), one can also notice that the latter shows a shift to lower kinetic energies and a decrease in intensity. Despite that, the effects around zero pump-probe delay are fully reproducible over all five consecutive acquisitions, as shown in Fig. 10, bottom right panel. These and further measurements will the subject of a separate paper.

The time resolution of the experiment is dominated by the pulse length of the X-ray beam, which is estimated to be about 60 ps FWHM for the camshaft bunch in hybrid mode operation [26]. The jitter between the laser and X-ray pulses as well as the cumulative error of the phase shifter over long delay scans have yet to be characterized systematically; first tests, however, point to overall effects not worse than 100 ps. As the ArTOF detector is sensitive to laser photons at 515 nm, the temporal overlap between the two beams at the sample could be determined by measuring with the ArTOF both the X-ray and laser photons, a simple and fast procedure which gives the time zero of the pump-probe delay scale with a precision better than 25 ps.

6. Conclusions

We have presented the PM4 beamline of BESSY II and its LowDosePES end-station, which is open to user operation since April 2015. The beamline layout and end-station instrumentation have been described and selected cases of study discussed to illustrate aspects where the angle-resolved time-of-flight electron spectrometer of which the station is endowed can make a difference.

In particular, the end-station is designed for photoemission spectroscopy investigations on samples that usually suffer from radiation damage – including for example technologically relevant photoactive organic materials – where a low irradiation dose is demanded, and that therefore particularly benefit from a high transmission spectrometer. Even when low photon flux is not a figure of merit, what can make the ArTOF favorable in a lot of circumstances is the wide angle acceptance providing the possibility of recording spectra all at once. So, in summary, while it is well probable that other instruments at other facilities will do better at efficiently measuring XPS on single crystals, our end-station can be a convenient choice when it comes to mapping the band structure of samples that are easily prone to damage or whose orientation is not know or not unique, since in such cases merging cuts in k space obtained at subsequent times for different sample rotations is a procedure that one would like to avoid as soon as there is the possibility.

The advantage is even more clear when an extra dimension has to be scanned, like in time-resolved experiments, and especially in pump-probe time-resolved experiments in combination with an ultrafast optical laser. Concerning the latter type of studies, the high repetition rate of both the X-ray and laser sources available at the LowDosePES is a major strength with respect to free electron lasers (FELs), as well as the wide energy range from 20 eV to 1.8 KeV is a major strength with respect to laser-based high harmonic generation (HHG) sources. On the other hand, the temporal resolution is not as high as at FEL and HHG facilities, which have to be the choice for the study of sub-picosecond dynamics. Time resolutions shorter by up to a factor 10 can be actually reached at today's synchrotrons in the so-called low-alpha mode of the storage ring [27], but only at a considerably reduced flux[3] and only for a couple of weeks per year at BESSY II. Producing X-ray pulses with lengths of few ps – thus longer than available at FELs and HHG sources but shorter than available at all other synchrotron sources now – at unaltered flux and routinely has been set as the goal of BESSY-VSR, a project for upgrading BESSY II to a variable pulse-length storage ring [28] to whose realization we are looking forward.

Acknowledgments

We thank Mike Sperling, Benjamin Dubrau, Christian Weniger and Dirk Ponwitz for engineering and technical contributions. We are grateful to Fredrik Johansson, Danilo Kühn, Ieva Bidermane, Valeria Lanzilotto and Bertrand Philippe for help during beamtimes. The research leading to these results has received funding from the European Research Council under the European Union's Seventh Framework Programme (FP7/2007–2013)/ERC grant agreement (n° 321319). We acknowledge financial contributions from Universität Potsdam within the project "CHOPTOF: MHz--Chopper für multidimensionale winkelaufgelöste Flugzeitspektroskopie an BESSY II" (BMBF--Projekt 05K12IP2). We thank Helmholtz--Zentrum Berlin für Materialien und Energie GmbH (HZB) and Helmholtz Association for funding. Svante Svensson and Nils Mårtensson received economic support from the Carl Tryggers Foundation (CTS) and the Swedish Research Council (VR). Yasmine Sassa was supported through the Wenner Gren foundation. Andreas Lindblad acknowledges the support from the Swedish Research Council (Grant no. 2014--6463) and Marie Sklodowska Curie Actions (Cofund, Project INCA 600398).

References

[1] S. Hüfner, Photoelectron Spectroscopy: Principles and Applications, third edition, Springer-Verlag, Berlin, 2003.
[2] C. Nordling, E. Sokolowski, K. Siegbahn, Phys. Rev. 105 (1957) 1676–1677.
[3] K. Siegbahn, C. Nordling, G. Johansson, J. Hedman, P.F. Hedén, K. Hamrin, U. Gelius, T. Bergmark, L.O. Werme, R. Manne, Y. Baer, ESCA Applied to Free Molecules, 1969 (North-Holland Amsterdam-London).
[4] C.N.K. Siegbahn, A. Fahlman, R. Nordberg, K. Hamrin, J. Hedman, G. Johansson, T. Bergmark, S.-E. Karlsson, I. Lindgren, B. Lindberg, ESCA Atomic Molecular and Solid State Structure Studied by Means of Electron Spectroscopy, Almqvist and Wiksells, Uppsala, 1967.
[5] S. Hagström, C. Nordling, K. Siegbahn, Physics Letters 9 (1964) 235–236.
[6] N. Martensson, E. Sokolowski, S. Svensson, J. Electron Spectrosc. Relat. Phenom. 193 (2014) 27–33.
[7] M.I. Al-Joboury, D.W. Turner, Journal of the Chemical Society (Resumed) (1963) 5141–5147.
[8] A. Damascelli, Z. Hussain, Z.-X. Shen, Rev. Mod. Phys. 75 (2003) 273.
[9] N. Koch, D. Pop, R.L. Weber, N. Böwering, B. Winter, M. Wick, G. Leising, I.V. Hertel, W. Braun, Thin Solid Films 391 (2001) 81–87.
[10] R. Ovsyannikov, P. Karlsson, M. Lundqvist, C. Lupulescu, W. Eberhardt, A. Fohlisch, S. Svensson, N. Martensson, J. Electron Spectrosc. Relat. Phenom. 191 (2013) 92–103.
[11] R. Follath, Nuclear Instruments and Methods in Physics Research A 467–468 (2001) 418–425.
[12] http://www.helmholtz-berlin.de/pubbin/igama_output?modus=einzel&sprache=en&gid=1614.
[13] M.A. MacDonald, F. Schaefers, R. Pohl, I.B. Poole, A. Gaupp, F.M. Quinn, Rev. Sci. Instrum. 79 (2008) 025108.
[14] A. Vollmer, O. Jurchescu, I. Arfaoui, I. Salzmann, T. Palstra, P. Rudolf, J. Niemax, J. Pflaum, J. Rabe, N. Koch, Eur. Phys. J. E 17 (2005) 339–343.
[15] D.F. Förster, B. Lindenau, M. Leyendecker, F. Janssen, C. Winkler, F.O. Schumann, J. Kirschner, K. Holldack, A. Föhlisch, Opt. Lett. 40 (2015) 2265–2268.
[16] K. Holldack, R. Ovsyannikov, P. Kuske, R. Muller, A. Schalicke, M. Scheer, M. Gorgoi, D. Kuhn, T. Leitner, S. Svensson, N. Martensson, A. Fohlisch, Nat. Commun. 5 (2014).
[17] C. Strahlman, R. Sankari, M. Lundqvist, G. Ohrwall, R. Ovsyannikov, S. Svensson, N. Martensson, R. Nyholm, J. Phys. Conf. Ser. 425 (2013).
[18] A. Bostwick, T. Ohta, T. Seyller, K. Horn, E. Rotenberg, Nat. Phys. 3 (2007) 36–40.

[3] In the current low-alpha mode, the bunches are 5–10 ps FWHM for currents between 2 and 30 μA/bunch [26].

[19] S.Y. Zhou, G.-H. Gweon, A.V. Fedorov, P.N. First, W.A. de Heer, D.-H. Lee, F. Guinea, A.H. Castro Neto, A. Lanzara, Nat. Mater. 6 (2007) 770–775.
[20] E. Moreau, S. Godey, X. Wallart, I. Razado-Colambo, J. Avila, M.-C. Asensio, D. Vignaud, Phys. Rev. B 88 (2013) 075406.
[21] A.H. Castro Neto, F. Guinea, N.M.R. Peres, K.S. Novoselov, A.K. Geim, Rev. Mod. Phys. 81 (2009) 109–162.
[22] F. Varchon, P. Mallet, J.-Y. Veuillen, L. Magaud, Phys. Rev. B 77 (2008) 235412.
[23] U. Bach, D. Lupo, P. Comte, J.E. Moser, F. Weissörtel, J. Salbeck, H. Spreitzer, M. Grätzel, Nature 395 (1998) 583–585.
[24] D. Bi, W. Tress, M.I. Dar, P. Gao, J. Luo, C. Renevier, K. Schenk, A. Abate, F. Giordano, J.-P.C. Baena, J.-D. Decoppet, S.M. Zakeeruddin, M.K. Nazeeruddin, M. Grätzel, Anders Hagfeldt Science Advances 2 (2016) 1501170.
[25] M. Bässler, A. Ausmees, M. Jurvansuu, R. Feifel, J.-O. Forsell, P. de Tarso Fonseca, A. Kivimäki, S. Sundin, S.L. Sorensen, R. Nyholm, O. Björneholm, S. Aksela, S. Svensson, Nucl. Instrum. Methods Phys. Res., Sect. A 469 (2001) 382–393.
[26] K. Holldack, private communication.
[27] J. Feikes, K. Holldack, P. Kuske, G. Wustefeld, Proceedings of EPAC 2004, Lucerne, Switzerland, 2004, pp. 2290–2292.
[28] BESSY VSR- Technical Design Study, June 2015 http://dx.doi.org/10.5442/R0001.